Nanostructure of Nanostructure of the Ionic Liquid-Graphite Stern Layer.

Aaron Elbourne,[1] Samila McDonald,[1] Kislon Voitchovsky,[2] Frank Endres,[3]

Gregory G. Warr,[4] and Rob Atkin[1,]*

[1] Discipline of Chemistry, The University of Newcastle, NSW 2308, Callaghan, Australia.

[2] Department of Physics, Durham University, Durham, England, United Kingdom.

[3] Institute of Particle Technology, Clausthal University of Technology, Arnold-Sommerfeld-Str. 6, 38678, Clausthal-Zellerfeld, Germany

[4] School of Chemistry, The University of Sydney, NSW 2006, Australia.

* Corresponding author

TOC GRAPHIC

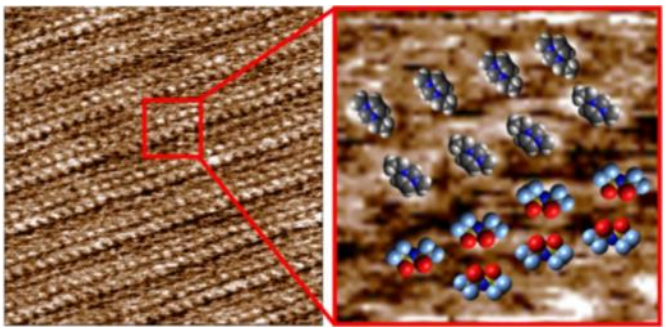

Abstract

Ionic liquids (ILs) are attractive solvents for devices such as lithium ion batteries and capacitors, but their uptake is limited, partially because their Stern layer nanostructure is poorly understood compared to molecular solvents. Here, in situ amplitude-modulated atomic force microscopy has been used to reveal the Stern layer nanostructure of the 1-ethyl-3-methylimidazolium bis(trifluoromethylsulfonyl)imide (EMIm TFSI)–HOPG (highly ordered pyrolytic graphite) interface with molecular resolution. The effect of applied surface potential and added 0.1 wt/wt % Li TFSI or EMIm Cl on ion arrangements is probed between ±1 V. For pure EMIm TFSI at open-circuit potential, well-defined rows are present on the surface formed by an anion–cation–cation–anion (A–C–C–A) unit cell adsorbed with like ions adjacent. As the surface potential is changed, the relative concentrations of cations and anions in the Stern layer respond, and markedly different lateral ion arrangements ensue. The changes in Stern layer structure at positive and negative potentials are not symmetrical due to the different surface affinities and packing constraints of cations and anions. For potentials outside ±0.4 V, images are featureless because the compositional variation within the layer is too small for the AFM tip to detect. This suggests that the Stern layer is highly enriched in either cations or anions (depending on the potential) oriented upright to the surface plane. When Li^+ or Cl^- is present, some Stern layer ionic liquid cations or anions (respectively) are displaced, producing starkly different structures. The Stern layer structures elucidated here significantly enhance our understanding of the ionic liquid electrical double layer.

Keywords:

ionic liquids; **amplitude-modulated atomic force microscopy**; **surface chemistry**; **self-assembly**; **adsorption**

Introduction

Ionic liquids (ILs) are pure salts with melting points below 100 °C.(1-5) ILs have many useful properties such as large electrochemical windows,(6, 7) low volatility,(5) and high thermal stability.(1) Many ILs are nanostructured on the length scale of the ions, both in the bulk(8-11) and at interfaces.(12-15) The bulk liquid structure of several protic(10) and aprotic(16) ILs has been elucidated by a combination of radiation scattering experiments(3, 17, 18) (X-ray and neutron) and computational studies.(19-21) IL nanostructure results from strong electrostatic attractions between the cation charge groups and anions, leading to the formation of polar domains. Cation alkyl chains are solvophobically excluded from these polar regions and cluster together to form segregated apolar regions. The polar and apolar domains percolate through the bulk liquid in a bicontinuous L_3 sponge structure. Generally, protic ILs are nanostructured for primary cations,(10) while aprotic ILs are nanostructured when the cation alkyl chain is 4 or more carbons long.(3)

Interest in aprotic ILs as electrochemical solvents can be attributed to their large electrochemical windows (up to ~6 V) and inherently high conductivity;(22, 23) protic ILs have narrower electrochemical windows and so are generally of less interest for electrochemistry.(24) However, the uptake of aprotic ILs for electrochemical devices, such as lithium ion batteries and capacitors, has been limited for several reasons but especially because the IL EDL (electrical double layer) is not as well-defined as for molecular solvents. The IL EDL cannot be described using the mean-field models (*e.g.*, Helmholtz,(25) Gouy–Chapman,(26, 27) and Stern(28)) because (1) ILs are pure electrolytes with Debye lengths smaller than the IL ion pair dimensions; (2) IL ions cannot be approximated as point charges or even small, charged spheres due to their large size and delocalized charge; (3) ILs possess charged and uncharged moieties that interact with solid surfaces through electrostatic attractions, van der Waals, and solvophobic forces; and (4) the solely ionic nature of ILs means that the concentration of charged species at the interface does not differ greatly from the bulk.

The IL EDL nanostructure normal to the interface has been extensively probed using several experimental techniques.(12-15) There is general agreement that the nanostructure is stronger near the surface than in the bulk due to the ordering effect of the substrate.(12) It is thought that IL ions interact strongly with solid surfaces to produce well-formed Stern layers that template structure in subsequent near surface layers. While

useful for applications such as lubrication, the strongly bound surface can lead to unpredictable electrochemical effects.(29) Applying a surface potential induces a reordering of the normal Stern layer structure to compensate the interfacial charge; the surface is enriched in anions at positive potentials and *vice versa*.(29-34) This behavior has been theoretically validated with several important computational studies modeling the IL–electrode interface.(30-37) In a landmark 2011 paper, Bazant *et al.*(38) predicted the potential-dependent normal distribution of ions with focus on overscreening and crowding of ions at electrode interfaces. Ion crowding occurs at high voltages when a single ion layer is insufficient to neutralize the surface potential. Overscreening is manifested at lower potentials when the charge of the Stern layer ions are greater than that of the electrode and is compensated by ions in the second layer.(38)

More recently, the importance of the lateral distribution of ions in the IL EDL has become apparent.(39-45) In a 2014 editorial, Kornyshev and Qiao(35) point out that recent computer simulations(30-37) and experimental studies(33, 46, 47) reveal that IL EDLs have rich three-dimensional structures that undergo voltage-driven structural transitions. They state that "*the structure of the double layer in RTILs, which just a year ago seemed to be majorly understood, still raises new puzzles and challenges*". Critically, they ask "*how the lateral arrangement of ions is coupled with their distribution in the perpendicular directions*". For a thorough review of these issues, the interested reader is directed to this editorial and the prior article by Merlet *et al.* which stimulated it.(34) In this work, we begin to address the three-dimensional ion arrangements in the IL EDL by revealing the lateral structure of the IL Stern layer *in situ* as a function of potential and added solute. In some instances, we are able to show coupling between the Stern and second ion layers. The Stern layer is defined as the ion layer in contact with the electrode surface, which is sometimes referred to in the IL literature as the "innermost" layer.(40-42)

Classically, scanning tunnel microscopy (STM)(43-45) has been used to investigate the IL EDL laterally but is unable to achieve atomic resolution at solid–IL interfaces because the strong interfacial liquid nanostructure interferes with the STM signal.(48) Molecular resolution can be achieved with STM for frozen IL monolayers under ultrahigh vacuum (UHV) conditions.(43-45) However, the structures determined almost certainly do not accurately represent the structure of the bulk IL–electrode interfaces. This is because in a monolayer the ions contact the electrode surface and a vacuum, rather than the surface

and the bulk liquid, which can lead to different ion orientations. Critically, in a monolayer, the ion ratio is also fixed at 1:1. This means that the monolayer nanostructure cannot accurately reflect the different affinities of the ions for the surface. Most importantly, realistic studies of the Stern layer structure as a function of potential for monolayers are impossible as the composition cannot change in response to an applied potential.

Video STM images of the bulk 1-butyl-1-methylpyrrolidinium bis[(trifluoromethyl)sulfonyl]amide (BMP TFSA–Au(111)) interface in the absence of solutes have been reported very recently.(49) While images were featureless for potentials higher than −1.0 V, between −1.0 and −1.6 V, adsorbed cations formed rows on the surface (anions could not be detected). It was postulated that rows were formed by cations adsorbed in a rectangular unit cell and that images could not be obtained for potentials greater than −1.0 V due to high cation mobility; stronger surface cation electrostatic interactions at lower potentials reduced the cation adlayer diffusion rates, enabling images to be obtained. At −1.4 V, the unit cell dimensions were 0.51 nm by 1.01 nm with an internal angle of 78°. When the potential was decreased to −1.6 V, the dimensions of the unit cell changed to 0.5 nm by 0.55 nm at right angles. These differences were attributed to the cation alkyl chain lying flat on the surface at −1.4 V and adopting an upright conformation at −1.6 V, which enables tighter cation packing on the gold surface.

We have recently used *in situ* amplitude-modulated atomic force microscopy (AM-AFM) to reveal the interfacial nanostructure of protic ILs on mica(39, 40, 42) and highly ordered pyrolytic graphite (HOPG) at open-circuit potential (OCP) (no applied potential).(41) Near molecular resolution was achieved for the bulk interface, enabling relationships between the IL molecular structure and interfacial nanostructure to be determined. In this paper, we use AM-AFM to examine the Stern layer structure for the interface of the aprotic IL EMIm TFSI with graphite. The structure of the IL cation and anion is shown in Figure 1 along with the approximate dimensions determined using Jmol. The effect of surface potential is probed between ±1.0 V with and without added 0.1 wt/wt % Li TFSI or EMIm Cl. These salts were chosen as they are electrochemically significant(50) and allow nanostructure cause–effect relationships to be established. Furthermore, both Li^+ and Cl^- have a strong influence on the double-layer structure in aqueous systems(51) and are known to alter the interfacial structure of ILs even at very low concentrations.(52) These

experiments reveal the arrangement of IL cations and anions on the surface for potentials between ±0.3 V as well as how added Li^+ or Cl^- affects the Stern layer structure.

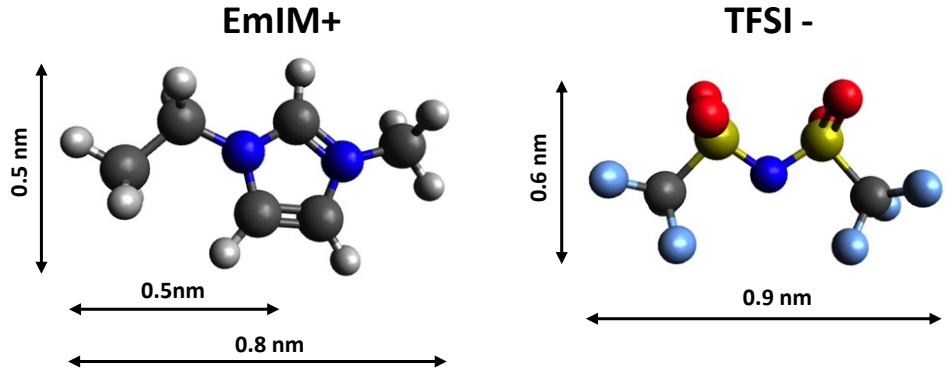

Figure 1. Structure and dimensions of EMIm TFSI. Carbon atoms are shaded grey, nitrogen is dark blue, hydrogen is silver, oxygen is red, sulphur is yellow and fluorine is light blue.

Methods

EMIm TFSI and EMIm Cl were purchased from Io-Li-Tec, Ionic Liquids Technologies, Germany, in the highest purity available (>99.9%). Analytical grade lithium TFSI was purchased from Sigma-Aldrich. 0.1 wt/wt% EMIm Cl or Li TFSI in EMIm TFSI solutions were prepared using an analytical balance, heated at ~60°C, and sonicated for several hours in a sealed vial to ensure complete dissolution. The water content of these ILs was undetectable by Karl Fisher titration (<0.01 v/v%). Highly ordered pyrolytic graphite (HOPG) surfaces were bought from NT-MDT Co., Russia, and cleaved along the basal plane using adhesive tape immediately prior to experiment. The freshly cleaved HOPG was therefore atomically smooth and clean.

The IL systems were studied using an Asylum Research Cypher Atomic Force Microscope (Cypher AFM). All data was obtained at a temperature of 25°C. Images were obtained using ArrowUHFAuD (NanoWorld, Switzerland, nominal spring constant k_c = 6 N m^{-1}) with cantilevers oscillating at (or close to) their resonant frequency. Each cantilever was calibrated using its thermal spectrum in IL prior to imaging and the lever sensitivity determined using force spectroscopy. Cantilever tips were irradiated with UV light for 15 minutes prior to experiment to remove organic contaminants. Experiments were completed in a droplet exposed to

the atmosphere within the AFM box (a sealed enclosure). As the IL is hygroscopic, the water content of the liquid increases over the course of an experiment. The data presented in this paper was obtained no more than 60 minutes after the IL droplet was placed on the HOPG. The Karl Fischer titration water content of IL collected from the cell after 60 minutes had a value of no more than ~1 wt% which depended slightly on the ambient humidity, so the water concentration in the data presented is <1%. The features of all images presented rotated as the scan angle was changed and scaled correctly with scan size, confirming they are not imaging artefacts. All dimensions provided are ±0.1 nm unless stated otherwise.

The standard droplet cell of the Cypher AFM was modified to obtain *in situ* electrochemical measurements. A thin (diameter ~0.25 mm) cylindrical strip of Cu and Pt wire were used as the counter electrode (CE) and "quasi"reference electrodes (QRE), respectively. The CE and QRE were cleaned in dilute HCl acid solution and then washed with Milli-Q water and dried in using a stream of nitrogen gas. HOPG was used as both the working electrode (WE) and the solid substrate for AFM experiments. The QRE and CE were located directly above the centre of the WE surface by securing the Pt and Cu wire to the droplet cell. Ohmic loss was minimized by positioning the QRE to as close as possible (<2 mm) to the WE surface. The potential of all electrodes was controlled by a WaveNow USB Potentiostat (model: WN50-BASIC). The samples were held at each potential for 8 minutes prior to data acquisition to ensure electrochemical equilibrium. *In situ* cyclic voltamagrams were obtained over a voltage window of ±1 V for all systems investigated and were in accordance with those obtained previously;[51] no electrochemical processes were observed over this voltage range. The OCP for the pure liquid, EMIm TFSI + Li TFSI 0.1 wt/wt% and EMIm TFSI + EMIm Cl 0.1 wt/wt% systems were 0.26 V vs. Pt, 0.30 V vs. Pt and 0.42 V vs. Pt, respectively.

During AM-AFM imaging a cantilever is excited by a piezoelectric actuator which induces the cantilever to oscillate. The cantilevers oscillation is controlled at a fixed, user set, amplitude and frequency (at or near the cantilevers first resonance frequency) which is monitored by a split photodiode detector. The IL surface structure is probed by imposing a cantilever amplitude, or setpoint (A), that is lower than the free liquid amplitude (A_0) which causes the cantilever to come into contact with the interface. The amplitude and phase of the cantilever was kept constant by a feedback loop that continuously adjusts the average tip-sample distance. The sample is then scanned line by line producing an image of the interface from the corrections

imposed by the feedback loop. Topography images are produced by monitoring the divergence of the AFM scanners z-axis from zero position. Simultaneously phase images are derived from the difference between the cantilevers zero phase signal and the surface perturbed phase signal. In these systems, the phase and amplitude vary in response to the liquid compliance between the tip and the surface. During imaging, values of $A/A_0 \geq 0.7$ were typically used with the free liquid amplitude (A_0) of the cantilever ≈ 1 nm. Using these parameters the cantilever is able to directly probe the Stern layer ions without interacting with the HOPG. It should be noted that the Stern layers in all systems are dynamic, with constant diffusion of ions in and out of the structures. The AM-AFM captures the average structure over the course of producing an image.

Results

Pure EMIm TFSI–HOPG System

AM-AFM phase and topography images of the EMIm TFSI–HOPG interface are presented in Figure 2. The 300 nm × 300 nm images are shown in Figure 2A,B. Higher magnification 30 nm × 30 nm images of the EMIm TFSI–HOPG interface are presented in Figure 2C,D, and the section bounded by the red box is enlarged in Figure 2E,F. Features are more clearly defined in phase images than topography images. This is because the AM-AFM phase signal is more sensitive to minor compositional variations than the topographic signal.(53) In the phase images, the dark areas indicate that the material between the tip and the surface is compliant, while lighter areas indicate relatively noncompliant (unyielding) matter.(54) In simple terms, compliant and noncompliant refers to matter that is relatively immobile or displaced from the space between the surface and AFM tip, but the explicit interpretation is much more complex.(54, 55)

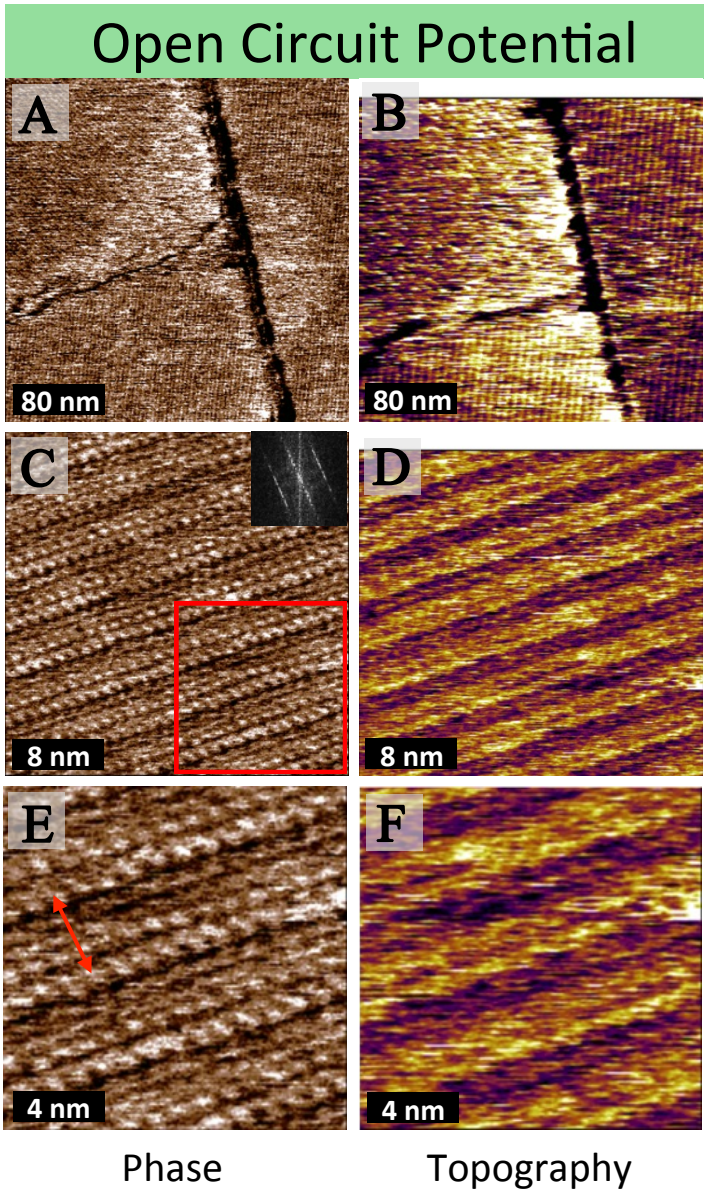

Figure 2. AM-AFM phase (mocha) and topographic (orange–violet–yellow) images of the IL Stern layer adsorbed to a graphite (HOPG) substrate. Image sizes are (A,B) 300 nm × 300 nm, (C,D) 30 nm × 30 nm, and (E,F) 15 nm × 15 nm. The interfacial images were collected at OCP (0.26 V *vs* Pt). The slow scan direction of all images is down the image. Fast Fourier transform of the phase image is shown as an inset. The red arrow indicates the larger repeat spacing of the image. The area in the red box in (C) is expanded in (E,F).

The 300 nm images reveal rows oriented at 60° to each other around grain boundaries at the graphite surface. The rows indicate that the Stern layer is laterally heterogeneous at OCP. Rows oriented around a grain boundary in this fashion have been reported previously for aqueous surfactant–HOPG interfaces due to adsorption of surfactant hemimicelles along one of graphite's three symmetry axes.(56, 57) While the dimensions of the surfactant hemimicelles are an order of magnitude larger, it appears the graphite is orienting the EMIm TFSI Stern layer in a similar fashion.

The topography images in Figure 2D,F reveal alternate rows of relatively noncompliant (light) and compliant (dark) material. The width of each row is ~2 nm, meaning that the structure repeats with a period of ~4 nm as indicated by the red arrow in Figure 2E. The row structure is much larger and of a different symmetry than the underlying HOPG surface, which has hexagonal symmetry and a lattice spacing of 0.246 nm.(58) The width of the rows is also significantly larger than the dimensions of individual IL cations or anions (*cf.* Figure 1).

The phase data in Figure 2C,E show that the rows are composed of smaller repeating structures. The rows in the noncompliant region are formed by discrete ellipses with major and minor axis lengths of ~0.8 and ~0.7 nm, respectively. These are arranged with square symmetry into two well-defined adjacent subrows. The fast Fourier transform (FFT, *cf.* inset Figure 2C) confirms this square symmetry(59) and reveals that the inter-ellipse (center-to-center) spacing is 1 nm both perpendicular and parallel to the row direction, consistent with measurements taken from the image. The structure between the ellipse double rows is less well-resolved, consistent with the material being more compliant. Two subrows can be identified, but discrete units are not particularly clear. The spacing between subrows is 1 nm.

Applying a potential to the graphite surface significantly alters the Stern layer structure (*cf.* Figure 3). In these experiments, the surface potential was changed in 0.1 V (*vs* OCP) increments and held at the specified potential until the appearance of the image was consistent. This was taken to mean that the structure was at equilibrium and generally required ~4 min. Equilibration times were similar when the magnitude of the potential change was larger. Structure changes were entirely reversible, and equilibration times were independent of the direction of the potential change. These results indicate that potential-induced ion rearrangements are facile processes. The images presented in Figure 3 were obtained at least 10 min after the potential was set but less than 60 min after the IL was contacted with the substrate. This ensures that the equilibrium structure is probed and that water contents remained low. Even after several hours, when the water content was ~3 wt %, the appearance of the image was consistent, indicating that small amounts of water do not effect the Stern layer structure for this system between ±0.3 V in a way that can be detected with AM-AFM.

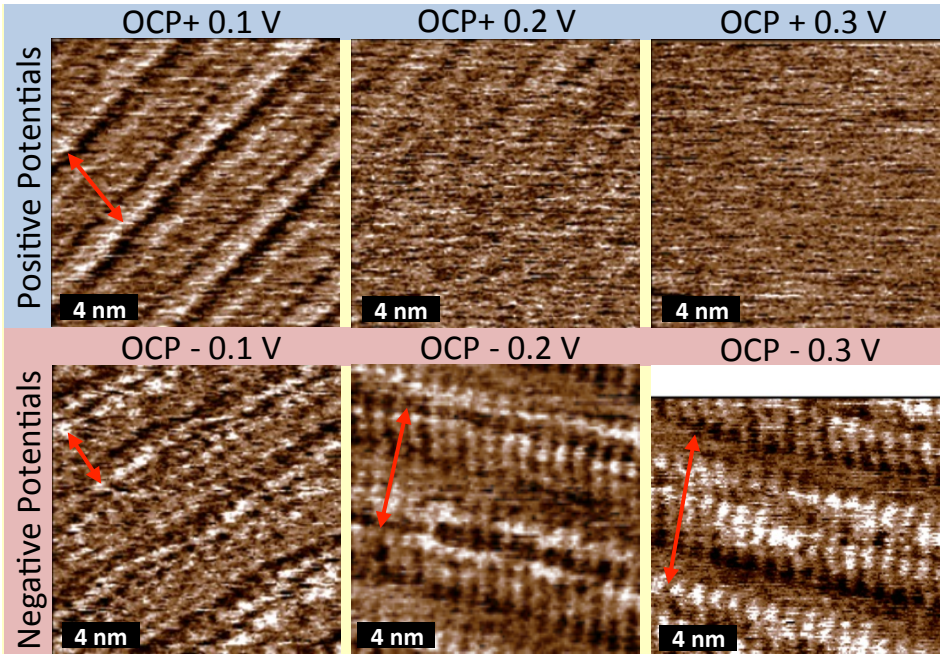

Figure 3. AM-AFM phase (mocha) images of the pure EMIm TFSI Stern layer adsorbed to a graphite (HOPG) substrate. Image sizes are all 15 nm × 15 nm. The interfacial data was collected at differing applied potentials (indicated in the figure). The slow scan direction of all images is down the image. The red arrow indicates the larger repeat spacing of the image.

Figure 3 shows 15 nm × 15 nm phase images of the EMIm TFSI–HOPG interface acquired at 0.1 V intervals on either side of OCP up to ±0.3 V. The corresponding height images (with the associated phase images reproduced) are shown in Figure A in the Supporting Information. When the potential is OCP + 0.1 V, the ellipse double row present at OCP is replaced by a single noncompliant row. Discrete structures cannot be resolved within the row, but its width is 1 nm, which is the same as the ellipses at OCP and suggests similar composition. Conversely, the width of the compliant region has increased from 2 nm at OCP to 3 nm at OCP + 0.1 V, meaning that the periodicity of the structure is constant at 4 nm at OCP and OCP + 0.1 V.

When the potential is increased from OCP by 0.1 V, the population of Stern layer anions and cations must increase and decrease, respectively. This means that the noncompliant rows in the images are Stern layer cations, while the compliant region is associated with (more difficult to discern) anions. As such, the ellipses in the OCP image indicate individual Stern layer cations, and the two rows in the compliant region are formed by anions. The dimensions of the cation ellipses and anion rows are consistent with the ion dimensions in Figure 1. On electrostatic grounds, it is expected that at OCP the numbers of cations and anions are approximately equal. These points are expanded upon in the Discussion.

The anion rows detected at OCP can no longer be discerned in the compliant region at OCP + 0.1 V. This indicates that the surface arrangement has become more disordered as the anion-rich region has grown larger. When the potential is further increased to OCP + 0.2 V, noncompliant cations are no longer observed, but there are hints of larger 2 nm structures which must be due to associated anions. Further increasing the potential to OCP + 0.3 V and above produces featureless images up to OCP + 1.0 V, the highest potential investigated.

The image obtained at OCP – 0.1 V consistently had a more disordered appearance than that obtained at OCP. When the potential is decreased, the population of cations and anions in the Stern layer must increase and decrease, respectively. At OCP – 0.1 V, the population of cation ellipses appears to have increased, but their arrangement is much less ordered than at OCP. This suggests that the relative cation and anion populations at OCP – 0.1 V do not permit well-ordered surface packing, and a disordered layer results.

Decreasing the potential to OCP – 0.2 V produces much larger and better defined structures than at OCP. Prominent 4 nm wide rows traverse the image separated by a 2 nm wide poorly defined compliant region, meaning that the overall structure repeats every 6 nm. A 30 nm × 30 nm image showing that these structures persist over larger distances is provided in the Supporting Information Figure B. Raised cation double rows 1.8 nm apart are present in the center of each large row. Additional narrow rows run the entire length of the images normal to the large row direction, aligned with the cations of the double row. The distance between cation ellipses (and thus the narrow rows) is 1 nm, the same as that between cations at OCP.

When the potential is further decreased to OCP – 0.3 V, the number of cations in the raised cation rows increases, and they are less compliant, resulting in larger and clearer structures. The overall width of the prominent rows has increased to ~5 nm, while the valleys are still 2 nm, resulting in an overall repeat length of 7 nm. In accordance with results at lower potentials, the cation repeat spacing along the large structures is 1 nm. At potentials less than OCP – 0.3 V, featureless images were obtained.

Effect of Lithium Cations

AM-AFM images of the EMIm TFSI + 0.1 wt/wt% Li TFSI–HOPG interface at OCP are shown in Figure 4. This Li TFSI concentration is the same as that in earlier work on the structure of the IL EDL normal to the

interface.(52, 60) The features in the image are markedly different than those observed for the pure IL, indicating the presence of Li^+ in the Stern layer, consistent with the affinity of Li^+ for the HOPG surface. The phase images reveal that the cation double rows present for the pure liquid have been replaced by 1 nm wide single ellipse rows. These single rows are separated by a less well-defined 4 nm wide depressed region, meaning the structure repeats every 5 nm. The diameter of Li^+ is 0.16 nm,(61) and in the high ionic strength IL, the physical size that the AM-AFM tip could potentially detect is expected to be of similar magnitude. As the width of the well-resolved ellipses in the noncompliant row is almost an order of magnitude larger than the Li^+ diameter, this suggests that the ellipses indicate the position of $EMIm^+$, as per the pure liquids, and that Li^+ in the Stern layer must be present in the large compliant domain.

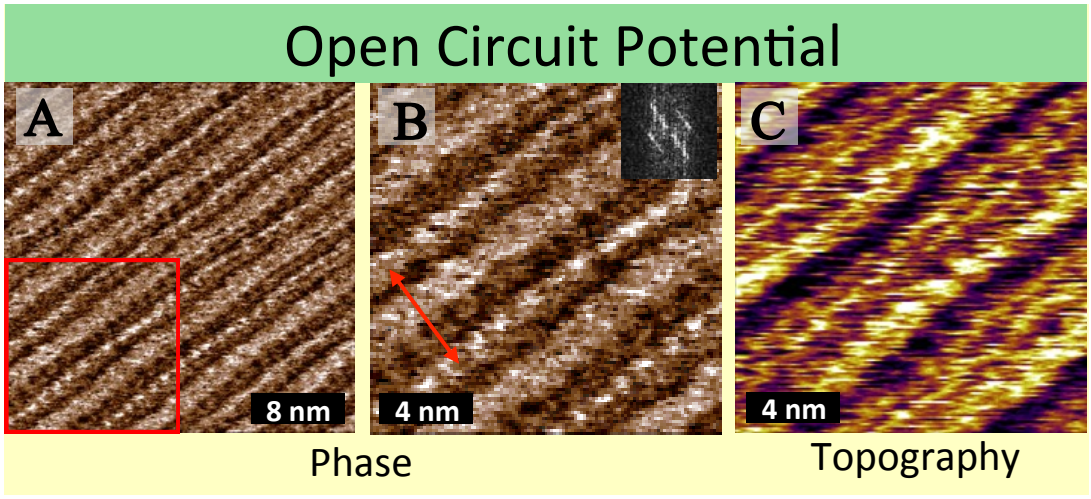

Figure 4. Figure 4. AM-AFM phase (mocha) and topographic (orange–violet–orange) images of the EMIm TFSI + 0.1 wt/wt % Li TFSI Stern layer adsorbed to a graphite (HOPG) substrate. The interfacial data were collected at OCP (0.31 V *vs* Pt). The slow scan direction of all images is down the image. The FFT of the phase image is shown as an inset. The area in the red box in (A) is expanded in (B,C).

The position of the Li^+ in the compliant domain cannot be determined from the phase images. As the Li^+ ion size is within the detection limit of AM-AFM imaging,(62) this means that the Li^+ and $TFSI^-$ must be strongly associated,(63) such that the tip interacts with the $TFSI^-$ which shields the buried Li^+. Given its small size and high affinity for HOPG, it is reasonable to assume that the Li^+ surface packing density is higher than that for the IL cations. However, in order to maintain electroneutrality, each Stern layer Li^+ must have a $TFSI^-$ anion associated with it. This leads to a compliant region wider than that in the pure IL at OCP and means that the anion limits the Li^+ surface packing density. The fact that no finer structure can be detected within this region means that the $TFSI^-$ anions are arranged irregularly.

Phase images of the EMIm TFSI + 0.1 wt/wt% Li TFSI–HOPG at 0.1 V potential intervals are shown in Figure 5. The corresponding height images (with the associated phase images reproduced) are shown in Figure C in the Supporting Information. When the potential is increased to OCP + 0.1 V, the structures in the image are unchanged within the detection limit from those at OCP. As the row features are associated with EMIm cations, the effect of the increase in potential must be to change the ion composition in the compliant region, with Li^+ ions repelled from the surface and replaced with $TFSI^-$ anions. When the potential is further increased, the regular detailed structure is lost; at OCP + 0.2 V, large irregular rows are noted that are somewhat reminiscent of those seen at the same potential in the absence of Li^+, and the image is essentially featureless at OCP + 0.3 V and above.

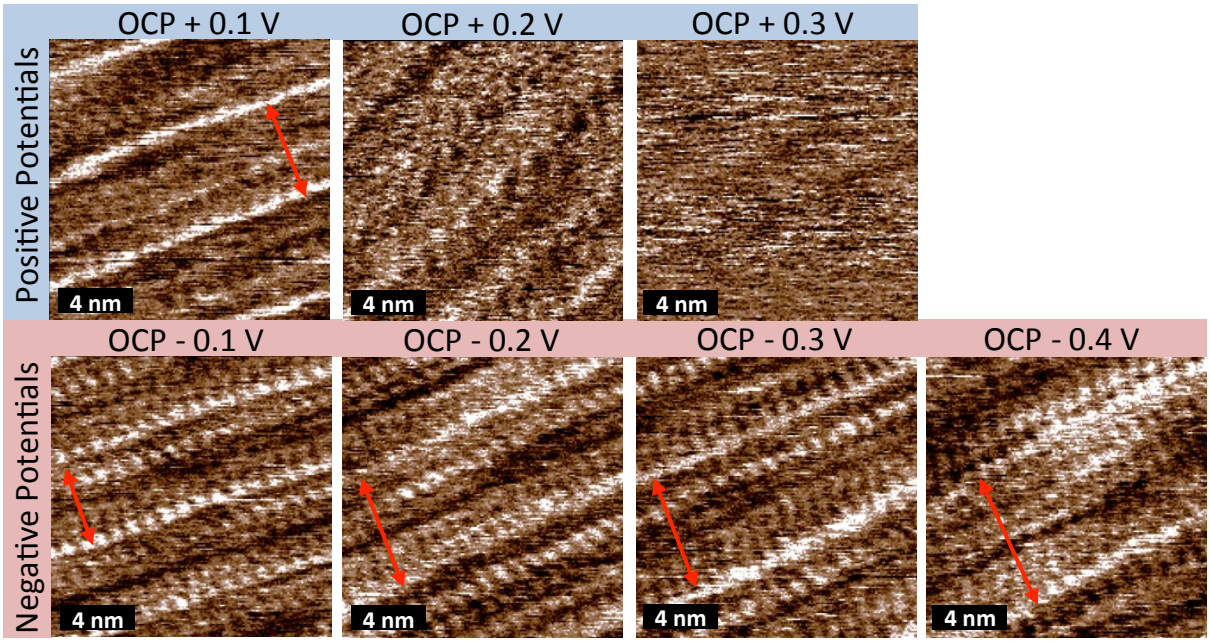

Figure 5. AM-AFM phase (mocha) images of the EMIm TFSI + 0.1 wt/wt % Li TFSI Stern layer adsorbed to a graphite (HOPG) substrate. Image sizes are all 15 nm × 15 nm. The interfacial data were collected at differing applied potentials (indicated in the figure). The slow scan direction of all images is down the image. The red arrow indicates the larger repeat spacing of the image.

When the potential is decreased to OCP – 0.1 V, the features in the image are significantly clearer than for EMIm TFSI + 0.1 wt/wt% Li TFSI–HOPG at OCP and is much more structured than the pure liquid at the same potential. This confirms that Li^+ is present in the Stern layer. The poorly resolved single cation rows present at OCP have been replaced by better defined (less compliant) cation double rows that are 2 nm wide,

and the width of the compliant region is reduced to 3 nm from 4 nm at OCP. Thus, while the structure repeats every 5 nm as it does at OCP, the anion-rich compliant region is 1 nm thinner in order to accommodate the extra $EMIm^+$ row. As seen previously, the regular arrangement of the cations produces rows running normal to the double row direction. These rows persist in the compliant region, which is better defined than at OCP.

When the potential is decreased further, the width of the rows increases while that of the compliant region decreases until, by OCP – 0.4 V, the thick rows (8 nm repeat spacing) constitute the entire surface. Unlike the pure EmIM TFSI at similar potentials, the cation rows do not appear to be as elevated, suggesting that a flatter Stern layer structure is facilitated by the presence of small Li^+ in the layer.

Effect of Chloride Anion

AM-AFM phase images for the EMIm TFSI + 0.1 wt/wt % EMim Cl–HOPG interface at OCP are shown in Figure 6. The corresponding height images (with the associated phase images reproduced) are shown in Figure D in the Supporting Information. In contrast to the OCP data for the pure IL and EMIm TFSI + Li TFSI 0.1 wt/wt %, the entire image of the Stern layer is well-defined, with no poorly resolved compliant regions. As these compliant regions are associated with $TFSI^-$ anions, this suggests that Cl^- has completely replaced $TFSI^-$ in the Stern layer. The repeating structure in this system consists of three cation rows separated by two rows of holes, as indicated by the blue box in Figure 6B. On a larger scale, this produces a repeating pattern of cation double rows, then a row of holes, followed by a cation single row and another row of holes. To maintain electroneutrality, the holes must contain negatively charged species. As in other systems, the $TFSI^-$ anion produces compliant features which are absent, and this suggests that Cl^- ions are present between the cation rows. The positions of the Cl^- ions appear as holes because either (1) they are displaced by the AFM tip during imaging or (2) their small size (the Cl^- diameter is 0.2 nm(61)) means that they sit below the imaging plane of the AFM tip which is determined by the heights of the adsorbed cations. To produce the observed alternating single/double cation rows, the surface area of Cl^- ions must be 33% less than that of EMIm ions, which is clearly possible given the physical size difference between the ions and the high ionic strength environment. This means that on average there is more than 1 Cl^- per hole and suggests that the holes result from the regular position of the larger cations but that single Cl^- anions are not resolved.

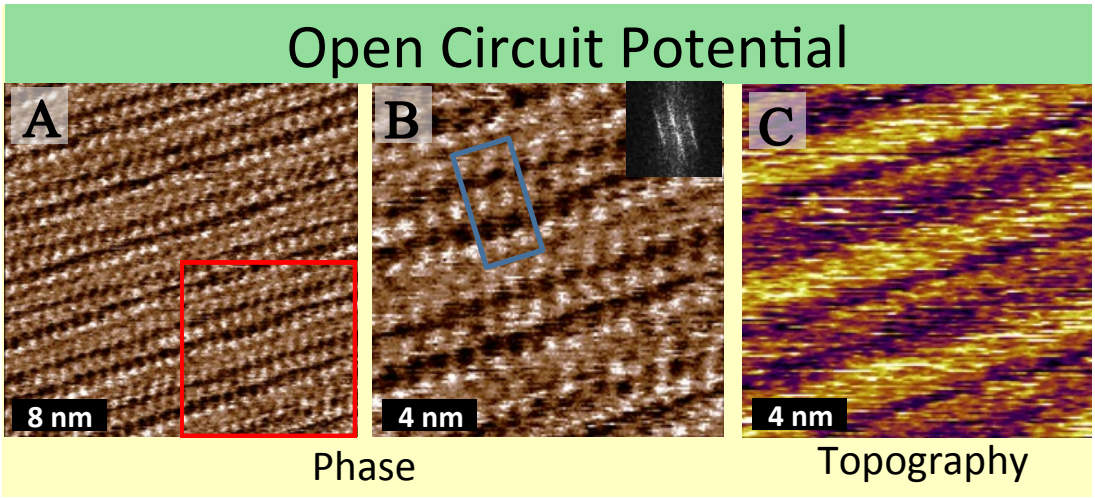

Figure 6. M-AFM phase (mocha) and topographic (orange–violet–yellow) images of the EMIm TFSI + 0.1 wt/wt % EMim Cl Stern layer adsorbed to a graphite (HOPG) substrate. The interfacial data were collected at OCP (0.42 V *vs* Pt). The slow scan direction of all images is down the image. The FFT of the phase image is shown as an inset. The area in the red box in (A) is expanded in (B,C). The blue box indicates the unit cell of the surface ions.

AM-AFM images for the EMIm TFSI + 0.1 wt/wt % EMIm Cl–HOPG interface as a function of potential are shown in Figure 7. When the potential is increased to OCP + 0.1 V, the multiple cation rows are replaced by single rows 5 nm apart and separated by a 4 nm wide compliant domain. This suggests that increasing the potential results in some cations being expelled from the Stern layer that are replaced with $TFSI^-$ and Cl^- anions. The proportion of the two anion types cannot be commented upon. Further increasing the potential to OCP + 0.2 V reveals cation rows. At first glance, this is counterintuitive given the surface potential but can be explained by a Cl^- layer bound to the surface with cations adsorbed on top. When the potential is increased to OCP + 0.3 V, the cation rows disappear and are replaced by much narrower rows that are only ~0.5 nm apart. At OCP + 0.4 V (not shown), similar images were obtained and featureless images were obtained at more positive potentials.

At OCP – 0.1 V, the interfacial layer structure is much less well-defined than at OCP. Low contrast (relatively cohesive) cation rows are present on top of a cation-rich layer. Cl^- must be present as the structure is both different and much better resolved than that of the pure IL at the same potential. It is likely that the small Cl^- allows the EMIm to pack tightly into a well-defined layer in contact with the surface. Additional cation double row layers are required to fully compensate the surface charge. The repeat spacing of these superstructure double rows is 4 nm. When the potential is decreased to OCP – 0.2 V, a similar structure is seen but with the upper double row repeat spacing decreased to 3 nm. This is consistent with

more cations being required to compensate the more negative potential. The upper rows are also less compliant, consistent with stronger binding due to the greater potential. There is no evidence that the structure of the ion layer in direct contact with the HOPG has changed. The appearance of these superstructure rows is different from those for the pure liquid, again indicating Cl^- is present. When the potential is further decreased to OCP – 0.3 V, the upper double rows become even more tightly packed (repeat spacing 2 nm) and the width of each individual row is reduced from 1 nm at OCP – 0.1 V to 0.5 nm at OCP – 0.3 V, suggesting cation reorientation within the rows.

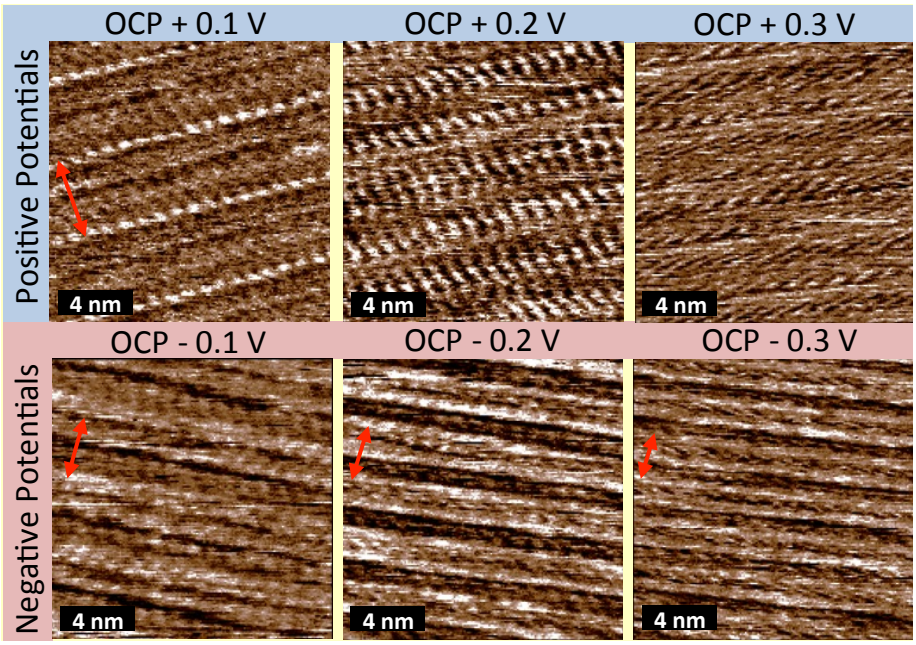

Figure 7. AM-AFM phase images of the EMIm TFSI + 0.1 wt/wt % EMim Cl Stern layer adsorbed to a graphite (HOPG) substrate. Image sizes are all 15 nm × 15 nm. The interfacial data were collected at differing applied potentials (indicated in the figure). The slow scan direction of all images is down the image. The red arrow indicates the larger repeat spacing of the image.

Discussion

The Stern layer of the EMIm TFSI–HOPG interface is sensitive to both applied potential and the presence of added lithium and chloride ions. The Stern layer commonly comprises single- or multiple-row structures of segregated cations and anions oriented by alignment with the underlying HOPG lattice. The double rows of cations and anions present for the pure EMIm TFSI–HOPG interface are much richer than the simple "checker board" structures reported for frozen monolayers of similar aprotic ILs by UHV STM,(43, 44)

highlighting the importance of multiple layers reaching into the adjacent bulk IL in determining structure.(12)

The spacing between individual $EMIm^+$ ions both along and between rows is 1 nm. This contrasts with a very recent video STM study of the bulk BMIm TFSI–Au(111) interface.(49) In that study, at −1 V, the same normal spacing was found, but the axial spacing was only 0.5 nm; at more negative potentials, the normal spacing was reduced to 0.5 nm. The large normal spacing for BMIm TFSI was attributed to association of cation butyl chains lying flat on the surface at −1.0 V, which decreases as the chains adopt a denser, upright conformation at more negative potentials. The larger cation spacing measured here (for all systems at all potentials), despite the shorter alkyl chain of $EMIm^+$, is attributed to the cation rotating in the plane of the interface. The shorter alkyl chain allows adsorbed cations to rotate about an axis near the center of the aromatic ring, which π–π stacks on HOPG aromatic rings.(31, 64) The distance from the center of the cation ring to the terminal hydrogen of the alkyl chain is 0.5 nm, which defines the rotating radius and accounts for the 1 nm spacing (see Figure 1).

The presence of double rows of cations and anions means that lateral attractions between like ions must be present, while still allowing the layer to pack in such a way as to satisfy charge neutrality in the unit cell. This segregation may be driven by ethyl chain association and polar/nonpolar segregation of groups in the cations or by the intrinsic immiscibility of fluorinated and hydrogenous groups on the anions and cations, respectively. In a double cation row, the ethyl chains can associate with neighboring Stern layer cations while undergoing restricted rotation; this could account for the cations appearing as ellipses rather than circles in the images (see, *e.g.*, Figure 2). (The long ellipse axis is not the same as the scan direction, so it is unlikely that the elongated shape is an imaging artifact.) Given the widespread use of fluorous anions in ILs, such double row structures may be common, and a systematic study of cation and anion structure variation may yield further insights into the Stern layer structure. In all images presented, the cations are better resolved than the anions. This is likely because the graphite surface interacts more strongly with the cations (*via* π–π stacking) than anions, and the flat cation geometry packs more effectively at the surface. Anions are less constrained and thus can adopt numerous interfacial geometries, meaning they are less well-resolved in images.

When the applied potential is increased, the Stern layer becomes enriched in anions, and this alters the lateral structure. At +0.1 V, the cation double rows are replaced by single rows, and the anion domain grows wider. However, this potential is not sufficient to overcome π–π attractions or displace all cations. Individual cation ellipses can no longer be detected because in a single row the cations have no preferred orientation. Similarly, as not all the $TFSI^-$ in the Stern layer is associated with a cation, orientational ordering of anions is lessened and rows cannot be detected. When the potential is further increased to OCP + 0.2 V, cation rows can no longer be detected in the image, although there are suggestions of larger structures which are due either to weak associations between Stern layer anions or to vestigial remnants of cation rows. At OCP + 0.3 V, the image is featureless, consistent with anions in the Stern layer packed in a dense but amorphous arrangement. In order to maximize electrostatic attractions, the anion central nitrogen will preferentially orient toward the HOPG surface, with fluorine groups facing into the bulk IL. This may account for the high lubricity observed for boundary layers composed of fluorine-rich anions.(29, 65) Fajardo *et al.*(37) have attempted to relate the lubricating properties of ILs to the interfacial ion arrangements.(37) Their simulation suggests that IL lubrication occurs *via* two mechanisms: (1) enrichment of a single ion species at the polarized interface (cations at negative potentials and *vice versa*), providing a smooth sliding plane; and (2) large surface potentials immobilizing ions sufficiently in several near surface layers to raise the slip plane, which prevents “squeeze-out” and interfacial wear. Importantly, the lateral surface-ion reordering and interfacial molecular geometry are key to achieving low-friction IL lubrication. While our results do not conclusively verify this interpretation, they are at least consistent with it.

The effect of negative applied potentials on structure is far from symmetrical. Although necessarily mirroring the enrichment of the Stern layer in counterions at positive potentials, the lateral structure evolves very differently. At OCP – 0.1 V, the Stern layer consists of a disordered arrangement of cation rows, seen as a high density of noncompliant ellipses. This suggests that at this potential the cation to anion ratio does not permit packing into a regular structure, so that the observed arrangement is the best compromise between the need for the ions to pack and the requirement to neutralize the surface potential.

In contrast with the amorphous (anion) layer seen at high positive potentials, decreasing potential to OCP – 0.2 V and beyond leads to the emergence of a well-defined superstructure of large cation double rows; the

corresponding height image (*cf*. Supporting Information Figure A) confirms that these doubles rows are elevated. Analysis of the height of phase images together reveals that cations (ellipses) are present at two distinct elevations, with the prominent rows on top of less well-defined underlayers. The rows are thus present to compensate the applied surface potential, which is not fully offset by the underlying cation film, due to attractions (including packing considerations) between ions in the underlayer and the superstructure, or some combination of both effects.

The relatively low surface potential may suggest that attractive interactions between ions play a key role, and the superstructure may thus overscreen the surface potential in line with previous predictions.(66) However, more cations are present at OCP – 0.3 V than at OCP – 0.2 V, and the rows are less compliant, suggesting that the surface potential is the dominant effect. In this work, we cannot categorically state whether overscreening occurs or not because the surface *charge* is not known. However, the double row superstructures observed for pure EMIm TFSI, and with added lithium or chloride, *could* be consistent with overscreening.

At large negative potentials, the 1.8 nm center-to-center distance between cations in the superstructure double rows is markedly larger than the 1 nm distance between cations in the surface-adsorbed double rows at OCP. This is attributed to a compliant anion row running between the cation double row in the superstructure. The additional 0.8 nm spacing is consistent with the physical dimensions of the $TFSI^-$ anion. Upon addition of 0.1 wt/wt % EMIm Cl at the same potentials, a similar superstructure occurs (Figure 7), but with a 1.2 nm row spacing due to the presence of the much smaller Cl^- between the double rows. For both systems, if ∼1 anion is present between every 2 cations, a net +1 positive charge remains available to compensate the surface potential. Packing considerations must make this cation–anion–cation row arrangement more favorable than a single row of cations, which would have approximately the same net charge.

Addition of 0.1 wt/wt % Li TFSI changes the appearance of Stern layer markedly from that of the pure liquid, with its effect most pronounced near and below OCP. The image at OCP is somewhat similar to pure EMIm TFSI at OCP + 0.1 V, with the cation double rows of the pure liquid replaced by single rows separated by a wider compliant region, as Li^+ replaces $EMIm^+$, and is present in the compliant region. Li^+

ions cannot be detected because of their strong association with the $TFSI^-$.(63) Discrete cations are apparent in the rows, which, based on the arguments above, suggests a preferred orientation. This suggests that the invisible Li^+ in the compliant region is arranged in a regular fashion in the center of HOPG rings.

Preliminary investigations of Li TFSI concentrations an order of magnitude higher and 2 orders of magnitude lower have revealed different structures from those reported here. These experiments will be described in a forthcoming publication but are mentioned to confirm that the Stern layer structure depends on the solute concentration, as expected; the surface excess of Li^+ will increase with concentration and negative applied potential until saturation is reached. Corresponding effects are expected for Cl^- and any other ion with appreciable surface affinity.

Increasing potential in the EMIm TFSI + 0.1 wt/wt % Li TFSI–HOPG system first expels Li^+, leading to a Stern layer similar to that found for pure EMIm TFSI at OCP. The $TFSI^-$ that was associated with the expelled Li^+ remains in the Stern layer and compensates the higher surface potential with no visible change in the structure. When the potential is further increased to OCP + 0.2 V, the structure becomes increasingly ill-defined, culminating in an amorphous layer of $TFSI^-$ only, similar to that observed in the absence of electrolyte.

At negative potentials, Li^+ in the Stern layer allows the cation double row structure preferred for the pure liquid at OCP to reassert itself. The position of Li^+ cannot be determined from the image, but it likely resides in the small anion-rich compliant regions between the rows. As the potential is further decreased, the Stern layer becomes more densely populated with cation rows, but the prominent double row superstructure present in the pure liquid does not form as enough Li^+ can pack into the $EMim^+$-rich Stern layer to satiate the surface potential without the need to form superstructure rows. At OCP – 0.4 V, the light shaded cation-rich areas may indicate the emergence of a second layer of elevated rows, but this structure is still much flatter than that in pure EMIm TFSI.

Addition of EMIm Cl strongly affects the structure of the interface. The OCP data for the EMIm TFSI + 0.1 wt/wt % EMIm Cl–HOPG system are the clearest of any system investigated in this study. The image indicates that Cl^- has completely displaced $TFSI^-$ in the Stern layer. The smaller Cl^- ions pack more tightly

on the HOPG than $TFSI^-$, meaning that less area is required to neutralize the charge of the cation. As a result, more cations are able to pack into the Stern layer, and the energetically favored packing structure is a repeating 2 $EMIm^+$ – 3 Cl^- – 2 $EMIm^+$ – 3 Cl^- – 2 $EMIm^+$ unit, as indicated by the blue box in Figure 6B. This adlayer structure maximizes cation–HOPG π–π stacking and solvophobic interactions between cation alkyl chains while preserving electroneutrality. The complex lateral structure generated by chloride addition serves to highlight the importance of polar/nonpolar segregation and the relative packing volumes of cations and anions in determining the lateral structure of the IL Stern layer. That is, the relative sizes of $TFSI^-$ and Cl^- have more impact on lateral structure than specific miscibility effects and should therefore be a primary control parameter for local order.

When the potential is increased to OCP + 0.1 V, the structure changes markedly. The single cation rows remain, but the cation double rows are repelled from the surface and replaced by anions that form a wide region. The compliance of the anion region suggests that it has an appreciable concentration of $TFSI^-$. The composition of the anion domain is determined by the relative surface affinities and bulk concentrations of $TFSI^-$ and Cl^-. If the bulk Cl^- concentration was increased, more Cl^- would be present in the Stern layer at this potential, which may lead to a better defined anion-rich domain.

At OCP + 0.2 V, a cation-rich layer is imaged, in stark contrast to the near featureless images noted for the other two systems at the same potential. On electrostatic grounds, this cannot be in contact with the HOPG surface at this potential. This suggests that a chloride-rich layer is in contact with the HOPG surface, and the cation is adsorbed either on top of or within this layer. Due to the small size of Cl^-, this cannot be resolved from the image. When the potential is increased to OCP + 0.3 V, poorly resolved rows only 0.5 nm across are imaged. The rows are not compliant, indicating that they are not due to $TFSI^-$, which therefore suggests a Cl^--only Stern layer. From the image, it cannot be stated whether one or more Cl^- layers are present on the HOPG, but given the small size of Cl^-, we suspect that a single layer of chloride ions is adsorbed at OCP + 0.3 V and that the cations may be embedded in the chloride layer at OCP + 0.2 V.

At OCP – 0.1 V, cation double rows are observed in a superstructure on top of a layer in contact with the surface in which only cations can be discerned. The small Cl^- ions allow $EMIm^+$ to pack neatly on the surface (unlike for the pure IL), but the potential of this layer is not sufficient to capacitatively match (or

almost match) the potential of the surface, resulting in the presence of the cation rows in the superstructure. The cation rows are not as elevated and less well-defined than those at OCP (at higher potentials) because, as described above, smaller Cl^- ions run down the center of the superstructure double rows instead of $TFSI^-$. This enables the $EMIm^+$ rows to pack more closely together and favors flatter orientations of the cation ring to the surface plane. When the potential is decreased further, no change can be detected in the ion layer in contact with the surface. The primary effect is that the repeat spacing of the superstructure double rows decreases monotonically from 4 nm at OCP – 0.1 V to 2 nm at OCP – 0.3 V. Thus, as the potential is decreased, more superstructure cation double layers (which have a net positive charge) are required to neutralize the surface potential, leading to closer packing. The uniform manner in which the packing density of the superstructure increases suggests that the underlayer composition remains relatively constant with potential over this range. At OCP – 0.3 V, the thickness of the individual cation rows in the double rows also decreases. This suggests that the cations adopt a more upright conformation (relative to the plane of the surface) to enable closer packing of cation double rows in the superstructure.

For all systems, featureless images are obtained when the potential is greater than OCP + 0.3 V or less than OCP – 0.4 V. This result is consistent with the molecular dynamic simulations of Merlet *et al.*,(34) which suggest that the first ion layer is ordered within a potential window of approximately 0.5 V but becomes disordered at higher and lower potentials.(34) It is likely that at positive potentials greater than OCP + 0.3 V the adsorbed layer is highly enriched in $TFSI^-$ (or Cl^- when present) with fluorine atoms oriented toward the bulk.(36, 44, 67) Fluorinated surfaces are lubricating, which makes imaging challenging. At potentials less than OCP – 0.4 V, cation rings are likely oriented relatively normal to the surface plane to maximize packing density and most effectively neutralize the surface charge. This leaves cation alkyl chains oriented toward the bulk liquid, so the imaging plane presented to the AM-AFM tip is a close-packed layer of C_2 alkyl chains. While these features of this size should be within the resolution of AM-AFM, the chains are not very tightly packed as the spacing is dictated by the size of the $EMIm^+$ ring. This means that the chains are compressed even under the weak imaging pressure of AM-AFM and therefore cannot be resolved.

Conclusions

A key driver of the remarkable surge in IL research interest in recent times is their potential as electrolytes in electrochemical devices such as batteries and capacitors and as solvents for electrodeposition. This interest was spurred by the attractive combination of physical properties exhibited by ILs, including high conductivity, electrochemical stability, inflammability, low vapor pressure, and solubilizing capacity, among others.(1, 5, 24) However, the use of ILs in devices and products is currently limited by the IL EDL being poorly understood compared to those of electrolyte solutions in molecular solvents.(22, 23) The normal structure of ILs near a solid surface is (relatively) easy to probe and is consequently well-characterized. However, the structure of the interfacial adlayer or Stern layer, which is critical for electrochemical processes,(22, 23) has proven to be much more difficult to examine *in situ* and is considerably less well-defined, especially its lateral structure across the surface. The work presented in this paper begins to bridge this knowledge gap.

The AM-AFM images presented in this work for the EMIM TFSI–HOPG interfaces resolve the positions of both cations and anions in the IL Stern layer *in situ* with ionic discrimination for the first time. The rich lateral structure revealed for the EMIM TFSI–HOPG Stern layer is very different than that determined for frozen monolayers of similar aprotic ILs by UHV STM(43, 44) and even more complex than predicted.(34, 35, 38, 68) Critically, the Stern layer nanostructure changes markedly with surface potential or when relatively low concentrations of lithium or chloride ions are present. The evolution of the Stern layer nanostructure at positive and negative potentials is asymmetrical. This reflects the different surface affinities, packing constraints, and charge localizations of the IL cations and anions; the Stern layer structure represents the best compromise between these effects and the surface potential, along with the solute concentration where applicable. At negative potentials for the pure liquid and in the presence of chloride, the AM-AFM images provide experimental evidence for the presence of an additional cation-rich layer on top of the ions in contact with the HOPG, which could overscreen the surface potential, as predicted in earlier indirect probes of Stern layer structure.(22)

Although the focus of this paper is the IL EDL, the (potential-dependent) structure of the IL layer in contact with a solid surface impacts upon a diverse range of process and applications including the use of ILs as lubricants,(29) colloid stability,(69) and dye solar cells.(7)

Supporting Information.

Additional AM-AFM images. The Supporting Information is available free of charge on the ACS Publications website at DOI: 10.1021/acsnano.5b02921..

Acknowledgements

R.A. thanks the Australian Research Council Future Fellowship (FT120100313). This research was supported by an Australian Research Council Discovery Project (DP120102708) and Equipment Grant (LE110100235). The authors would like to thank an anonymous reviewer for helpful suggestions.

References

1. Welton, T.Room-Temperature Ionic Liquids. Solvents for Synthesis and Catalysis Chem. Rev. 1999, 99, 2071– 2083
2. Greaves, T. L.; Weerawardena, A.; Fong, C.; Krodkiewska, I.; Drummond, C. J.Protic Ionic Liquids: Solvents with Tunable Phase Behavior and Physicochemical Properties J. Phys. Chem. B 2006, 110, 22479– 22487
3. Hardacre, C.; Holbrey, J. D.; Nieuwenhuyzen, M.; Youngs, T. G. A.Structure and Solvation in Ionic Liquids Acc. Chem. Res. 2007, 40, 1146– 1155
4. Wilkes, J. S.A Short History of Ionic Liquids: From Molten Salts to Neoteric Solvents Green Chem. 2002, 4, 73– 80
5. Earle, M. J.; Seddon, K. R.Ionic Liquids. Green Solvents for the Future Pure Appl. Chem. 2000, 72, 1391– 1398

6. Endres, F.; Hofft, O.; Borisenko, N.; Gasparotto, L. H.; Prowald, A.; Al-Salman, R.; Carstens, T.; Atkin, R.; Bund, A.; El Abedin, S. Z.Do Solvation Layers of Ionic Liquids Influence Electrochemical Reactions? Phys. Chem. Chem. Phys. 2010, 12, 1724– 1732
7. Gorlov, M.; Kloo, L.Ionic Liquid Electrolytes for Dye-Sensitized Solar Cells Dalton Trans. 2008, 2655– 2666
8. Hardacre, C.; Holbrey, J. D.; Mullan, C. L.; Nieuwenhuyzen, M.; Youngs, T. G. A.; Bowron, D. T.Liquid Structure of the Ionic Liquid, 1-Methyl-4-cyanopyridinium bis{(trifluoromethyl)sulfonyl}imide Determined from Neutron Scattering and Molecular Dynamics Simulations J. Phys. Chem. B 2008, 112, 8049– 8056
9. Hardacre, C.; Holbrey, J. D.; Mullan, C. L.; Youngs, T. G. A.; Bowron, D. T.Small Angle Neutron Scattering from 1-Alkyl-3-methylimidazolium hexafluorophosphate Ionic Liquids ([Cnmim][PF6], n=4, 6, and 8) J. Chem. Phys. 2010, 133, 074510
10. Hayes, R.; Imberti, S.; Warr, G. G.; Atkin, R.Effect of Cation Alkyl Chain Length and Anion Type on Protic Ionic Liquid Nanostructure J. Phys. Chem. C 2014, 118, 13998– 14008
11. Triolo, A.; Russina, O.; Bleif, H. J.; Di Cola, E.Nanoscale Segregation in Room Temperature Ionic Liquids J. Phys. Chem. B 2007, 111, 4641– 4644
12. Hayes, R.; Warr, G. G.; Atkin, R.At the Interface: Solvation and Designing Ionic Liquids Phys. Chem. Chem. Phys. 2010, 12, 1709– 1723
13. Perkin, S.Ionic Liquids in Confined Geometries Phys. Chem. Chem. Phys. 2012, 14, 5052– 5062
14. Perkin, S.; Albrecht, T.; Klein, J.Layering and Shear Properties of an Ionic Liquid, 1-Ethyl-3-methylimidazolium Ethylsulfate, Confined to Nano-films between Mica Surfaces Phys. Chem. Chem. Phys. 2010, 12, 1243– 1247
15. Perkin, S.; Crowhurst, L.; Niedermeyer, H.; Welton, T.; Smith, A. M.; Gosvami, N. N.Self-Assembly in the Electrical Double Layer of Ionic Liquids Chem. Commun. 2011, 47, 6572– 6574
16. Canongia Lopes, J. N. A.; Padua, A. A. H.Nanostructural Organization in Ionic Liquids J. Phys. Chem. B 2006, 110, 3330– 3335
17. Hardacre, C.; Holbrey, J. D.; McMath, S. E. J.; Bowron, D. T.; Soper, A. K.Structure of Molten 1,3-Dimethylimidazolium Chloride Using Neutron Diffraction J. Chem. Phys. 2003, 118, 273– 278

18. Hardacre, C.; McMath, S. E. J.; Nieuwenhuyzen, M.; Bowron, D. T.; Soper, A. K.Liquid Structure of 1,3-Dimethylimidazolium Salts J. Phys.: Condens. Matter 2003, 15, S159– S166
19. Li, H.; Endres, F.; Atkin, R.Effect of Alkyl Chain Length and Anion Species on the Interfacial Nanostructure of Ionic Liquids at the Au (111) -Ionic Liquid Interface as a Function of Potential Phys. Chem. Chem. Phys. 2015, 15, 14624– 14633
20. Freitas, A. A.; Shimizu, K.; Canongia Lopes, J. N.Complex Structure of Ionic Liquids. Molecular Dynamics Studies with Different Cation–Anion Combinations J. Chem. Eng. Data 2014, 3120– 3129
21. Kowsari, M. H.; Alavi, S.; Ashrafizaadeh, M.; Najafi, B.Molecular Dynamics Simulation of Imidazolium-Based Ionic Liquids. Dynamics and Diffusion Coefficient J. Chem. Phys. 2008, 129, 224508
22. Fedorov, M. V.; Georgi, N.; Kornyshev, A. A.Double Layer in Ionic Liquids: The Nature of the Camel Shape of Capacitance Electrochem. Commun. 2010, 12, 296– 299
23. Fedorov, M. V.; Kornyshev, A. A.Ionic Liquids at Electrified Interfaces Chem. Rev. 2014, 114, 2978– 3036
24. Greaves, T. L.; Drummond, C. J.Protic Ionic Liquids: Properties and Applications Chem. Rev. 2008, 108, 206– 237
25. von Helmholtz, H.The Double Layer Wied. Ann. 1879, 7, 337
26. Gouy, G.Constitution of the Electric Charge at the Surface of an Electrolyte J. Phys. Theor. Appl. 1910, 9, 457– 467
27. Chapman, D. L.A Contribution to the Theory of Electrocapillarity Philos. Mag. 1913, 25, 475– 481
28. Stern, O.Zur Theorie der Elektrolytischen Doppelschicht Elektrochem. 1924, 30, 508– 516
29. Li, H.; Rutland, M. W.; Atkin, R.Ionic Liquid Lubrication: Influence of Ion Structure, Surface Potential and Sliding Velocity Phys. Chem. Chem. Phys. 2013, 15, 14616– 14623
30. Pounds, M.; Tazi, S.; Salanne, M.; Madden, P. A.Ion Adsorption at a Metallic Electrode: An Ab Initio Based Simulation Study J. Phys.: Condens. Matter 2009, 21, 424109
31. Kislenko, S. A.; Amirov, R. H.; Samoylov, I. S.Molecular Dynamics Simulation of the Electrical Double Layer in Ionic Liquids J. Phys.: Conf. Ser. 2013, 418, 012021

32. Tazi, S.; Salanne, M.; Simon, C.; Turq, P.; Pounds, M.; Madden, P. A.Potential-Induced Ordering Transition of the Adsorbed Layer at the Ionic Liquid/Electrified Metal Interface J. Phys. Chem. B 2010, 114, 8453– 8459

33. Jha, K. C.; Liu, H.; Bockstaller, M. R.; Heinz, H.Facet Recognition and Molecular Ordering of Ionic Liquids on Metal Surfaces J. Phys. Chem. C 2013, 117, 25969– 25981

34. Merlet, C.; Limmer, D. T.; Salanne, M.; van Roij, R.; Madden, P. A.; Chandler, D.; Rotenberg, B.The Electric Double Layer Has a Life of Its Own J. Phys. Chem. C 2014, 118, 18291– 18298

35. Kornyshev, A. A.; Qiao, R.Three-Dimensional Double Layers J. Phys. Chem. C 2014, 118, 18285– 18290

36. Black, J. M.; Walters, D.; Labuda, A.; Feng, G.; Hillesheim, P. C.; Dai, S.; Cummings, P. T.; Kalinin, S. V.; Proksch, R.; Balke, N.Bias-Dependent Molecular-Level Structure of Electrical Double Layer in Ionic Liquid on Graphite Nano Lett. 2013, 13, 5954– 5960

37. Fajardo, O. Y.; Bresme, F.; Kornyshev, A. A.; Urbakh, M.Electrotunable Lubricity with Ionic Liquid Nanoscale Films Sci. Rep. 2015, 5, 7698

38. Bazant, M. Z.; Storey, B. D.; Kornyshev, A. A.Double Layer in Ionic Liquids: Overscreening *versus* Crowding Phys. Rev. Lett. 2011, 106, 046102

39. Elbourne, A.; Sweeney, J.; Webber, G. B.; Wanless, E. J.; Warr, G. G.; Rutland, M. W.; Atkin, R.Adsorbed and Near-Surface Structure of Ionic Liquids Determines Nanoscale Friction Chem. Commun. 2013, 49, 6797– 6799

40. Elbourne, A.; Voitchovsky, K.; Warr, G. G.; Atkin, R.Ion Structure Controls Ionic Liquid Near-Surface and Interfacial Nanostructure Chem. Sci. 2015, 6, 527– 536

41. Page, A. J.; Elbourne, A.; Stefanovic, R.; Addicoat, M. A.; Warr, G. G.; Voitchovsky, K.; Atkin, R.3-Dimensional Atomic Scale Structure of the Ionic Liquid-Graphite Interface Elucidated by AM-AFM and Quantum Chemical Simulations Nanoscale 2014, 6, 8100– 8106

42. Segura, J. J.; Elbourne, A.; Wanless, E. J.; Warr, G. G.; Voitchovsky, K.; Atkin, R.Adsorbed and Near Surface Structure of Ionic Liquids at a Solid Interface Phys. Chem. Chem. Phys. 2013, 15, 3320– 3328

43. Buchner, F.; Forster-Tonigold, K.; Uhl, B.; Alwast, D.; Wagner, N.; Farkhondeh, H.; Groß, A.; Behm, R. J.Toward the Microscopic Identification of Anions and Cations at the Ionic Liquid|Ag(111) Interface: A Combined Experimental and Theoretical Investigation ACS Nano 2013, 7, 7773– 7784

44. Uhl, B.; Cremer, T.; Roos, M.; Maier, F.; Steinruck, H.-P.; Behm, R. J.At the Ionic Liquid|Metal Interface: Structure Formation and Temperature Dependent Behavior of an Ionic Liquid Adlayer on Au(111) Phys. Chem. Chem. Phys. 2013, 15, 17295– 17302

45. Waldmann, T.; Huang, H.-H.; Hoster, H. E.; Höfft, O.; Endres, F.; Behm, R. J.Imaging an Ionic Liquid Adlayer by Scanning Tunneling Microscopy at the Solid|Vacuum Interface ChemPhysChem 2011, 12, 2565– 2567

46. Su, Y.-Z.; Fu, Y.-C.; Yan, J.-W.; Chen, Z.-B.; Mao, B.-W.Double Layer of Au(100)/Ionic Liquid Interface and Its Stability in Imidazolium-Based Ionic Liquids Angew. Chem. Int. Ed. 2009, 121, 5250– 5253

47. Anderson, E.; Grozovski, V.; Siinor, L.; Siimenson, C.; Lust, E.*In Situ* STM Studies of Bi(111)|1-Ethyl-3-methylimidazolium Tetrafluoroborate/1-Ethyl-3-methylimidazolium Iodide Interface Electrochem. Commun. 2014, 46, 18– 21

48. Pan, G.-B.; Freyland, W.2D Phase Transition of PF_6 Adlayers at the Electrified Ionic Liquid/Au(111) Interface Chem. Phys. Lett. 2006, 427, 96– 100

49. Wen, R.; Rahn, B.; Magnussen, O. M.Potential-Dependent Adlayer Structure and Dynamics at the Ionic Liquid/Au(111) Interface: A Molecular-Scale *In Situ* Video-STM Study Angew. Chem., Int. Ed. 2015, 54, 6062– 6066

50. Endres, F.; Borisenko, N.; Al Salman, R.; Al Zoubi, M.; Prowald, A.; Carstens, T.; El Abedin, S. Z. Electrodeposition from Ionic Liquids: Interface Processes, Ion Effects, and Macroporous Structures. Ionic Liquids Uncoiled; John Wiley & Sons, Inc.: New York, 2012; pp 1– 27.

51. Israelachvili, J. Intermolecular and Surface Forces, 3rd ed.; Academic Press: New York, 2010.

52. Hayes, R.; Borisenko, N.; Corr, B.; Webber, G. B.; Endres, F.; Atkin, R.Effect of Dissolved LiCl on the Ionic Liquid–Au(111) Electrical Double Layer Structure Chem. Commun. 2012, 48, 10246– 10248

53. García, R. Amplitude Modulation Atomic Force Microscopy; Wiley-VCH Verlag GmbH & Co. KGaA: Weinheim, Germany, 2010; pp 91– 101.

54. Voitchovsky, K.; Kuna, J. J.; Contera, S. A.; Tosatti, E.; Stellacci, F.Direct Mapping of the Solid–Liquid Adhesion Energy with Subnanometre Resolution Nat. Nanotechnol. 2010, 5, 401– 405

55. Voitchovsky, K.; Ricci, M. High-Resolution Imaging of Solvation Structures with Amplitude-Modulation Atomic Force Microscopy. Conference on Colloidal Nanocrystals for Biomedical Applications VII, SPIE: San Francisco, CA, 2012; Vol. 8232.

56. Manne, S.; Gaub, H. E.Molecular Organization of Surfactants at Solid–Liquid Interfaces Science 1995, 270, 1480– 1482

57. Manne, S.; Cleveland, J. P.; Gaub, H. E.; Stucky, G. D.; Hansma, P. K.Direct Visualization of Surfactant Hemimicelles by Force Microscopy of the Electrical Double Layer Langmuir 1994, 10, 4409– 4413

58. Albrecht, T. R.; Quate, C. F.Atomic Resolution Imaging of a Nonconductor by Atomic Force Microscopy J. Appl. Phys. 1987, 62, 2599– 2602

59. Harburn, G.; Taylor, C. A.; Welberry, T. R. Atlas of Optical Transforms; Cornell University Press: Ithaca, NY, 1975.

60. Endres, F.; Borisenko, N.; El Abedin, S. Z.; Hayes, R.; Atkin, R.The Interface Ionic Liquid(s)/Electrode(s): *In Situ* STM and AFM Measurements Faraday Discuss. 2012, 154, 221– 233

61. Cotton, F. A.; Wilkinson, G.; Murillo, C. A.; Bochmann, M.; Grimes, R. Advanced Inorganic Chemistry; Wiley: New York, 1999; 6th ed.

62. Ricci, M.; Spijker, P.; Stellacci, F.; Molinari, J.-F.; Voïtchovsky, K.Direct Visualization of Single Ions in the Stern Layer of Calcite Langmuir 2013, 29, 2207– 2216

63. Lahiri, A.; Schubert, T. J.; Iliev, B.; Endres, F.LiTFSI in 1-Butyl-1-methylpyrrolidinium Bis(fluorosulfonyl)amide: A Possible Electrolyte for Ionic Liquid Based Lithium Ion Batteries Phys. Chem. Chem. Phys. 2015, 17, 11161– 11164

64. Baldelli, S.Probing Electric Fields at the Ionic Liquid–Electrode Interface Using Sum Frequency Generation Spectroscopy and Electrochemistry J. Phys. Chem. B 2005, 109, 13049– 13051

65. Li, H.; Wood, R. J.; Rutland, M. W.; Atkin, R.An Ionic Liquid Lubricant Enables Superlubricity To Be “Switched On” *In Situ* Using an Electrical Potential Chem. Commun. 2014, 50, 4368– 4370

66. Kornyshev, A. A.Double-Layer in Ionic Liquids: Paradigm Change? J. Phys. Chem. B 2007, 111, 5545– 5557

67. Atkin, R.; Abedin, S. Z. E.; Hayes, R.; Gasparotto, L. H. S.; Borisenko, N.; Endres, F.AFM and STM Studies on the Surface Interaction of [BMP]TFSA and [EMIm]TFSA Ionic Liquids with Au(111) J. Phys. Chem. C 2009, 113, 13266– 13272

68. Kirchner, K.; Kirchner, T.; Ivaništšev, V.; Fedorov, M. V.Electrical Double Layer in Ionic Liquids: Structural Transitions from Multilayer to Monolayer Structure at the Interface Electrochim. Acta 2013, 110, 762– 771

69. Szilagyi, I.; Szabo, T.; Desert, A.; Trefalt, G.; Oncsik, T.; Borkovec, M.Particle Aggregation Mechanisms in Ionic Liquids Phys. Chem. Chem. Phys. 2014, 16, 9515– 9524

70. Wallauer, J.; Drüschler, M.; Huber, B.; Roling, B.The Differential Capacitance of Ionic Liquid| Metal Electrode Interfaces: A Critical Comparison of Experimental Results with Theoretical Predictions Z. Naturforsch. B 2013, 68, 1143– 1153